Biochimica et Biophysica Acta 1840 (2014) 535–544

Contents lists available at ScienceDirect

Biochimica et Biophysica Acta

journal homepage: www.elsevier.com/locate/bbagen

The *Salmonella enterica* ZinT structure, zinc affinity and interaction with the high-affinity uptake protein ZnuA provide insight into the management of periplasmic zinc

Andrea Ilari [a,1], Flaminia Alaleona [a,1], Giancarlo Tria [c,d], Patrizia Petrarca [b,e], Andrea Battistoni [b,e], Carlotta Zamparelli [a], Daniela Verzili [a], Mattia Falconi [b,e], Emilia Chiancone [a,*]

[a] CNR Institute of Molecular Biology and Pathology and Department of Biochemical Sciences, "Sapienza" University of Rome, Piazzale A. Moro 5, 00185 Rome, Italy
[b] Department of Biology, University of Rome "Tor Vergata" and CIBB, Center of Biostatistics and Bioinformatics, Via della Ricerca Scientifica, 00133 Rome, Italy
[c] European Molecular Biology Laboratory, Hamburg Outstation, c/o DESY, Notkestraße 85, Hamburg 22603, Germany
[d] Centre for Bioinformatics, University of Hamburg, Bundesstrasse 43, D-20146 Hamburg, Germany
[e] Interuniversity Consortium, National Institute Biostructures and Biosystems (INBB), Rome, Italy

ARTICLE INFO

Article history:
Received 18 July 2013
Received in revised form 17 September 2013
Accepted 7 October 2013
Available online 12 October 2013

Keywords:
Salmonella enterica
Zinc transport
Zinc affinity
Protein-protein interaction
SAXS
Analytical ultracentrifugation

ABSTRACT

Background: In Gram-negative bacteria the ZnuABC transporter ensures adequate zinc import in Zn(II)-poor environments, like those encountered by pathogens within the infected host. Recently, the metal-binding protein ZinT was suggested to operate as an accessory component of ZnuABC in periplasmic zinc recruitment. Since ZinT is known to form a ZinT–ZnuA complex in the presence of Zn(II) it was proposed to transfer Zn(II) to ZnuA. The present work was undertaken to test this claim.
Methods: ZinT and its structural relationship with ZnuA have been characterized by multiple biophysical techniques (X-ray crystallography, SAXS, analytical ultracentrifugation, fluorescence spectroscopy).
Results: The metal-free and metal-bound crystal structures of *Salmonella enterica* ZinT show one Zn(II) binding site and limited structural changes upon metal removal. Spectroscopic titrations with Zn(II) yield a K_D value of 22 ± 2 nM for ZinT, while those with ZnuA point to one high affinity ($K_D < 20$ nM) and one low affinity Zn(II) binding site (K_D in the micromolar range). Sedimentation velocity experiments established that Zn(II)-bound ZinT interacts with ZnuA, whereas apo-ZinT does not. The model of the ZinT–ZnuA complex derived from small angle X-ray scattering experiments points to a disposition that favors metal transfer as the metal binding cavities of the two proteins face each other.
Conclusions: ZinT acts as a Zn(II)-buffering protein that delivers Zn(II) to ZnuA.
General significance: Knowledge of the ZinT–ZnuA relationship is crucial for understanding bacterial Zn(II) uptake.

1. Introduction

Zinc (Zn) is the second most abundant transition metal after iron in living organisms where it plays vital roles. In bacteria, Zn has a catalytic function in a large number of housekeeping enzymes or virulence-related ones (*e.g.* β-lactamases or extracellular metalloproteinases) and a structural role in other enzymes (*e.g.* periplasmic copper, zinc superoxide dismutase). On the other hand, Zn at high concentrations is highly toxic for all cell types since it can interact non-specifically with polypeptide chains [1] and in that way inhibit essential enzymes [2]. It follows that the cellular concentration of Zn, as well as that of other metals like iron, has to be controlled very strictly. Bacteria achieve the delicate balance between the requirement for Zn and its toxicity by the coordinated action of high- and low-affinity uptake systems and of export systems that rid the cells of excess Zn. Thus, different transporters acquire the metal from the growth medium to reach a total concentration in the submillimolar range, while transcriptionally controlled zinc uptake and efflux systems maintain the readily exchangeable "free" zinc at very low concentrations [3]. Whereas initial *in vitro* studies suggested that cellular "free" zinc levels are in the femtomolar range [3], more recent studies involving ratiometric zinc biosensors have shown that the *in vivo* "free" zinc is around 20 pM [4].

Investigations carried out on *Escherichia coli*, and confirmed for other microorganisms like *Salmonella enterica*, have established that the activity of the Zn import and export systems is controlled by Zur and ZntR, two metalloproteins that regulate gene transcription depending on their metallation state. Zur comes into play when the Zn concentration in the medium is low [5]; it is known to control the expression of the high affinity Zn uptake system ZnuABC, which is used by Gram-

* Corresponding author. Tel.: +39 06 4940543.
E-mail address: emilia.chiancone@uniroma1.it (E. Chiancone).
[1] The authors contributed equally to the work.

0304-4165/$ – see front matter © 2013 Elsevier B.V. All rights reserved.
http://dx.doi.org/10.1016/j.bbagen.2013.10.010

negative bacteria to transport Zn from the periplasmic space to the cytosol. ZnuABC is a high affinity ATP-binding cassette-type transporter and like all such systems is composed of three proteins: a soluble periplasmic component (ZnuA) that captures Zn(II) and delivers it to the membrane permease (ZnuB), whereas the ATPase component (ZnuC) provides the energy necessary for ion transport through the inner membrane.

Panina et al. [6] identified other Zur-regulated genes interspersed within the bacterial chromosome. These include the gene for a putative metal-binding protein named ZinT, categorized initially as a member of the *E. coli* cadmium stress stimulon [7]. ZinT was proposed to decrease the cadmium concentration in *E. coli* cells during cadmium stress. This putative function was ruled out by later studies which indicated clearly that ZinT is involved in Zn homeostasis [8–11]. In particular, *Salmonella* and *E. coli* strains deleted of the *zinT* gene were shown to be impaired in their ability to grow in media poor of this metal [10,11]; moreover, ZinT accumulation was shown to depend on zinc availability in the medium. As in the case of ZnuA, *zint* expression increases in bacteria growing in Zn-poor media and is repressed in the presence of abundant Zn. Importantly, the expression of *zint* is deregulated in bacteria lacking ZnuA, but not *vice-versa*. As a result, bacteria lacking the *zint* gene are able to grow in a medium with low zinc concentrations, despite the reduced duplication rates, whereas bacteria lacking the *znua* gene are unable to grow [10,11]. These results indicate that the ZinT and ZnuABC activities are strictly related and that ZinT may be considered an accessory member of the ZnuABC transporter. The tight linkage between ZinT and the ZnuA and ZnuB components of the transporter is evidenced also by other experimental data. *Salmonella* mutant strains deleted either of the whole *znuABC* operon or of the single *znuA* gene—and thus potentially able to express ZnuB, but not ZnuA—are equally impaired in the ability to import environmental zinc [10]. It follows that ZnuB cannot mediate Zn(II) import in the absence of ZnuA. Further, ZinT cannot compensate for the lack of ZnuA, indicating that the role of ZinT is likewise dependent on the presence of ZnuA [10].

The data on the structural basis of this functional relationship are limited. It has been established that ZinT and ZnuA do not interact when metal-free, but form a stable complex when metal-bound [10]. However, the dependence of complex formation on the metallation state of the individual proteins and the mode of their interaction are not known. Interestingly, in some Gram-positive bacteria, Zn(II) transport is ensured by AdcA, a lipoprotein constructed by two domains resembling ZnuA and ZinT [6,12].

Even though several bacteria relying on the ZnuABC transporter to import Zn(II) do not possess ZinT, these studies suggest that the contribution of ZinT to metal recruitment within the periplasmic space is considerable, at least under conditions of severe Zn shortage and provided ZnuA is present [10]. It may be hypothesized that the ZinT contribution to Zn(II) recruitment entails binding of the metal with high affinity, followed by formation of a complex with ZnuA that allows metal to be transferred. To prove this contention, we have chosen to work on the proteins from *S. enterica* in view of the wealth of data accumulated in recent years on the ZnuABC transporter from this microorganism [10,13–15].

Firstly, X-ray crystal structure studies on *S. enterica* ZinT (*Se*ZinT) in the metal-free and metal-bound forms were undertaken. The only ZinT structure known pertains to metal-bound *E. coli* ZinT (*Ec*ZinT, indicated originally as YodA) [16]. *Ec*ZinT is composed of two domains: a major one related structurally to the lipocalin/calycin protein family and a smaller helical domain. The metal-binding site, formed by histidine side chains, is buried at the domain interface, along the side of the calycin domain [16]. It was not established whether the binding of Zn(II) gives rise to protein conformational changes.

In contrast to the ZinT proteins, the X-ray structures of several members of the ZnuA family are known, namely those of the proteins from *E. coli* (*Ec*ZnuA, PDB codes: 2OGW; 2OSV; 2PRS) [17–19], *Synechocystis 6803* (PDB code: 1PQ4) [20] and *S. enterica* (*Se*ZnuA, PDB code: 2XQV) [13]. The ZnuA family belongs to the so-called cluster 9 of periplasmic solute-binding proteins (PBPs) and displays their well conserved architecture comprising a pair of $(\alpha/\beta)_4$ sandwich domains and a connecting long, tightly packed α-helix. The distinctive characteristic of all ZnuA proteins consists of a histidine rich (His-rich) loop located at the entrance of the Zn(II) binding site at the interface between the two domains. The *Se*ZnuA structures with the Zn(II) binding site occupied either partially or fully, and the structure of a deletion mutant lacking a large part of the loop (*Se*ZnuA Δ118–141), where the site is empty (PDB code: 2XH8), all indicate that the His-rich loop plays an important role in the Zn(II) management process. In fact, their comparison unveiled for the first time the occurrence of Zn(II)-induced conformational changes that are likely of functional relevance in metal sequestration from the periplasm and/or its delivery to ZnuB. In particular, His140, placed on the C-terminal part of the *Se*ZnuA His-rich loop, appears of importance as it replaces His60 (*Ec*ZnuA numbering) [13], one of the otherwise conserved metal binding histidine residues in Zn- and Mn-specific PBPs. Moreover, structural–dynamical investigations pointed to a high mobility of the His-rich loop and suggested that the fluctuations may be influenced by Zn(II) binding either at the primary site or at the His-rich loop itself [14].

The hypothesis that the contribution of ZinT to the Zn(II) management processes in the *S. enterica* periplasm is based on its interaction with ZnuA and on the subsequent transfer of bound Zn(II) to the latter protein is strengthened by the data presented in this paper. Thus, the X-ray structures of metal-free and Zn(II)-bound *Se*ZinT disclose Zn(II)-induced conformational changes that are confined to the area surrounding the Zn(II) binding site. An additional Zn(II)-bound *Se*ZinT structure was solved that displays a PEG molecule in the inter-domain cleft, in a similar position as that occupied by the *Se*ZnuA His-rich loop in the model of the *Se*ZinT–Zn(II)–*Se*ZnuA complex derived from SAXS experiments. In the modeled complex the Zn(II) binding sites of the two proteins face each other, in an arrangement that allows metal to be transferred. Significantly, *Se*ZnuA has a higher affinity for the metal (K_D < 20 nM) than SeZinT (K_D 22 ± 2 nM) and the interaction of ZinT with ZnuA takes place only when Zn(II) is bound to ZinT.

2. Material and methods

2.1. Protein purification

Cells harboring plasmid pSEzinT [10] were grown at 37 °C in LB medium supplemented with 100 μg/ml ampicillin. Protein expression was induced overnight with 0.1 mM isopropyl β-D-1-thiogalattopiranoside (IPTG) when the absorbance of the culture at 600 nm reached 0.5. Cells were harvested by centrifugation for 15 min at 5000 rpm and periplasmic proteins were extracted by lysozyme treatment. Spheroplasts were separated from periplasmic proteins by centrifugation and the supernatant was applied to a Ni-NTA column pre-equilibrated with 50 mM Na–phosphate, 250 mM NaCl, pH 7.8 and eluted with a linear gradient of 0–500 mM imidazole. ZinT eluted at 250 mM imidazole, due to the presence of a naturally occurring His-rich N-terminal sequence which confers to the protein the ability to strongly interact with immobilized metal ions. Fractions containing ZinT (>98% pure according to SDS-PAGE analyses) were pooled, dialyzed against 20 mM HEPES, 10 mM NaCl, pH 7.0, concentrated to 20 mg/ml by ultrafiltration, using Amicon Ultrafiltration Discs YM-10, and stored at −20 °C. About 20 mg of purified protein was obtained per liter of bacterial culture. The protein concentration has been evaluated using the extinction coefficient at 280 nm ($\varepsilon = 37{,}485\ M^{-1}\ cm^{-1}$) based on the protein amino acid composition (http://web.expasy.org/tools/protparam/protparam-doc.html). Wt *Se*ZinT contains the signal peptide typical of periplasmic proteins and has 215 amino acids, whereas the recombinant protein comprises 186 residues. In the X-ray structure (see below) the first residues (HGHHAHGA) are not visible.

*Se*ZnuA and the metal-free protein were obtained as described by Petrarca et al. [10].

2.2. Protein crystallization, data collection and data processing

All *Se*ZinT crystals were grown in about 2 weeks at 25 °C by the hanging-drop vapor diffusion method, using a protein sample concentrated to ~20 mg/ml. *Se*ZinT crystals were obtained by mixing 1 μl of protein sample with an equal amount of reservoir solution containing 2 M ammonium sulfate and 0.1 M sodium acetate, pH 5.0.

The Zn(II)–*Se*ZinT and Zn(II)–*Se*ZinT–PEG co-crystals were obtained upon addition of zinc acetate to a 20 mg/ml protein sample at an ion/protein molar ratio of 5:1. The protein samples (1 μl) were mixed with an equal amount of reservoir solution containing respectively 1.5 M ammonium sulfate, 0.1 M sodium acetate, pH 4.6 or 0.22 M ammonium sulfate, 0.1 M sodium acetate, pH 4.6 and 25%–30% PEG 4000. The crystals were cryo-protected in a solution containing 80% (v/v) mother liquor and 20% (v/v) glycerol. For transport to the synchrotron-radiation source and data collection, the crystals were mounted in nylon loops and flash frozen by quick submersion into liquid nitrogen. Three single-wavelength data sets ($\lambda = 0.918$ Å) were collected from a *Se*ZinT crystal and from co-crystals of Zn(II)–*Se*ZinT and Zn(II)–*Se*ZinT–PEG at the BL-14.1 beam-line of the Synchrotron Radiation Source BESSY (Berlin, Germany) [21], using a MAR Mosaic 225 CCD detector at 100 K. The *Se*ZinT and Zn(II)–*Se*ZinT data sets were processed with DENZO [22] and scaled with SCALEPACK [22] while the Zn(II)–*Se*ZinT–PEG data set was processed with MOSFLM [23]. All the measured crystals belong to the P6122 space group. Crystal parameters and data collection statistics for the measured crystals are reported in Table 1.

2.3. Solution and refinement of the X-ray structures

All the structures were solved using *Ec*ZinT in complex with zinc (PDB entry: 1OEK) as search model. *Ec*ZinT displays 71.76% sequence identity with *Se*ZinT (calculated using the program CLUSTALW2 [24]). The rotational and translational searches, performed with the program MOLREP [25], CCP4 suite [26] in the resolution range 3.0–10.0 Å, produced clear solutions, corresponding to one monomer in the asymmetric unit. Refinements were performed using the maximum likelihood method with the program REFMAC [27] and model building with the program COOT [28]. The refinement statistics are reported in Table 1. The quality of the models was assessed using the program PROCHECK [29].

The final *Se*ZinT model consists of 186 residues, 136 water molecules, and 6 sulfate ions. The model has been refined to an R_{crys} of 22.05% and an R_{free} of 28.84%. The final Zn(II)–*Se*ZinT model consists of 186 residues, 77 water molecules, 4 sulfate ions and 1 zinc ion. The model has been refined to an R_{crys} of 23.38% and an R_{free} of 32.20%. The final Zn(II)–*Se*ZinT–PEG model consists of 186 residues, 150 water molecules, 5 sulfate ions, 1 zinc ion, and 1 PEG molecule ($C_{12}H_{26}O_7$). The final R_{crys} is 21.24% and R_{free} is 25.69%.

Table 1
Crystal parameters, data collection statistics and refinement statistics.

	*Se*ZinT	Zn(II)–*Se*ZinT	Zn(II)–*Se*ZinT–PEG
Data collection			
PDB code	4arh	4ayh	4aw8
Space group	P6122	P6122	P6122
Unit cell parameters	a = 58.53 Å b = 58.53 Å c = 289.32 Å γ = 120°	a = 58.40 Å b = 58.40 Å c = 291.47 Å γ = 120°	a = 58.54 Å b = 58.54 Å c = 290.37 Å γ = 120°
Resolution shell (Å)	2.3–50.00 (2.30–2.38)	2.5–99 (2.5–2.59)	2.00–50.70 (2.00–2.11)
*R_{merge} (%)	11.2 (23.7)	18.3 (46.8)	10 (23.7)
I/σ (I)	25.62 (14.75)	15.2 (3.83)	16.30 (8.90)
Unique reflections	14,007	10,654	21,245
Completeness (%)	99.1 (99.9)	97.9 (100)	100 (100)
Redundancy	12.7 (14.3)	5.8 (7)	11 (10.2)
Refinement statistics			
R_{factor} (%)	22.05	23.38	21.24
R_{free} (%)	28.84	32.2	25.69
FOM	0.79	0.77	0.84
RMS bonds	0.012	0.018	0.011
RMS angles	1.284	1.611	1.244
Ramachandran analysis			
Number of residues in:			
Favored region	178 (96.7%)	179 (97.3%)	177 (96.2%)
Allowed region	6 (3.3%)	5 (2.7%)	7 (3.8%)
Outliers	0 (0.0)%	0 (0.0)%	0 (0.0)%

Values in parentheses are for the highest-resolution.
$R_{merge} = \sum_{hkl}\sum_i |I_i(hkl) - I(hkl)| / \sum_{hkl}\sum_i I_i(hkl)$, where $I_i(hkl)$ is the ith observation of the reflection (hkl) and I(hkl) is the mean intensity of the (hkl) reflection.

2.4. Determination of the SeZinT and SeZnuA affinities for Zn(II)

Binding of Zn(II) to *Se*ZinT was followed by measuring the intrinsic protein fluorescence on a Fluoromax-4 spectrofluorometer (Horiba-Jobin Yvon). Fluorescence spectra were collected at 25 °C using 1 cm path length cell, under continuous stirring. The excitation wavelength was 280 nm, and emission was recorded between 300 and 450 nm. ZinT was equilibrated with 20 mM HEPES, 10 mM NaCl, pH 7.5 treated previously with Chelex 100 to avoid metal contamination. ICP-MS analysis confirmed that the *Se*ZinT:Zn molar ratio was <0.01. The same buffer was used to dilute the protein solution to a final concentration of 5 μM. A stock solution of zinc was prepared from atomic absorption standard (Fluka) diluted with ultra-pure water (Fluka). The metal was added to the protein in 0.15 μM increments.

Zinc binding to *Se*ZnuA was followed in indirect titration experiments in the presence of the indicator Mag-Fura-2, MF (Invitrogen) essentially as described in [19]. Absorption spectra were collected on a Hewlett–Packard diode array spectrophotometer at 25 °C. Freshly prepared MF was added to a solution of 20 mM HEPES, 10 mM NaCl, pH 7.5 to reach a final concentration of 16 μM and a reference spectrum was collected. The absorbance maximum of MF occurs at 366 nm, with an extinction coefficient of 29,900 M^{-1} cm^{-1}. When MF is bound to Zn(II) the absorbance maximum is shifted to the blue (325 nm) and the extinction coefficient at 366 nm decreases to 1880 M^{-1} cm^{-1} [30]. The dissociation constant of zinc from MF, K_D, is 20 nM at pH 7.0 [31]. *Se*ZnuA was added to the MF containing buffer at a final concentration of 20 μM; the aliquots of the Zn(II) stock solution described above were from 1 to 25 μM.

The overall Zn(II) dissociation constant, K_D, was obtained by fitting the experimental data obtained for both *Se*ZinT and *Se*ZnuA with a program written with Matlab (The Math Works, Natick, MA).

2.5. Analytical ultracentrifugation

Sedimentation velocity experiments were carried out on a Beckman Optima XL-I analytical ultracentrifuge using absorbance optics. Experiments were conducted at 30,000 rpm and 20 °C. Radial absorbance scans were obtained in a continuous scan mode at 280 nm at a spacing of 0.003 cm; three scans were averaged. Sedimentation coefficients were calculated using the program Sedfit (provided by P. Schuck, National Institutes of Health) and were reduced to water and 20 °C ($s_{20,w}$) using standard procedures. The samples were diluted in 20 mM HEPES,10 mM NaCl, pH 7.5 to reach an absorbance at 280 nm of 0.6 AU in a 1.2 cm optical path cell. When required, *Se*ZinT (22.2 kDa) and *Se*ZnuA (31.5 kDa) were mixed in a 1:1 molar ratio either in the apo- or in the holo-, Zn(II)-bound form.

2.6. Small angle X-ray scattering

Synchrotron X-ray scattering data were collected at the beamline BM29 (ESRF, Grenoble) [32] using a robot sample changer [33]. The

*Se*ZnuA–*Se*ZinT complex was measured at several concentrations ranging from 0.17 to 5.0 mg/ml in a HEPES buffer 20 mM, 10 mM NaCl, pH = 7.5. SAXS data were recorded at 4 °C using a Pilatus 1 M pixel detector (DECTRIS, Baden, Switzerland) at a sample detector distance of 2.43 m, covering the range of momentum transfer $0.005 < s < 0.45$ Å^{-1} ($s = 4\pi \sin(\theta)/\lambda$ where 2θ is the scattering angle and $\lambda = 0.931$ Å is the X-ray wavelength). To assess radiation damage, ten successive 1 s exposures of complex solutions were compared and no significant changes were observed (data not shown). The forward scattering $I(0)$ as well as the radius of gyration (R_g) were calculated using the Guinier approximation [34] implemented in PRIMUS [35,36] and assuming that at very small angles ($s < 1.3/R_g$) the intensity is represented as $I(s) = I(0)\cdot\exp(-(sR_g)^2/3)$. The pair-distance distribution function $P(r)$, from which the maximum particle dimension (D_{max}) as well as R_g were estimated, was computed using GNOM [37]. The molecular mass (*MM*) was estimated from: (1) the Porod invariant [38] as 0.5 times the Porod volume for roughly globular particles [36], (2) the excluded volume of averaged hydrated particles computed using DAMAVER [39], and (3) the comparison of the forward scattering $I(0)$ with that of the well characterized bovine serum albumin (BSA) ($MM_{BSA} = 66$ kDa, $I(0)_{BSA} = 69.184$) [40]. *Ab initio* models using low resolution data in the range of 0.012 Å$^{-1} < s < 0.22$ Å^{-1} were created using DAMMIF [41]. The tool constructs bead models keeping beads interconnected and the model compact while yielding a scattering profile with the lowest possible discrepancy (χ) to the experimental data

$$\chi^2 = \frac{1}{N-1}\sum_{j=1}^{N}\left[\frac{I_{exp}(s_j) - cI_{calc}(s_j)}{\sigma(s_j)}\right]^2 \quad (1)$$

where N is the number of experimental points, c is a scaling factor and $I_{calc}(s_j)$ and $\sigma(s_j)$ are respectively the calculated intensity and the experimental error at the momentum transfer s_j. Twelve independent *ab initio* reconstructions were performed and then averaged using DAMAVER [39], which also provides a value of normalized spatial discrepancy (NSD) representing a measure of similarity among different models (for ideally superimposed similar objects, NSD tends to 0; it exceeds 1 if the objects differ systematically from one another). Rigid body modeling was performed using MASSHA [42]. The tool allows one to display and manipulate atomic structures and low resolution models minimizing the discrepancy value χ (formula (1)) against the experimental data. Lastly, the program BUNCH [43] was used to model the missing loop as a chain of dummy residues that are separated by 3.8 Å (to mimic a C_α chain). The theoretical scattering curve was computed by CRYSOL [44] and the final model super-imposed on the *ab initio* model using the program SUPCOMB [45]. All programs used for SAXS data analysis belong to the ATSAS package [36].

3. Results

3.1. SeZinT: structural analysis

Three different crystal structures were solved pertaining to *Se*ZinT as purified (at 2.3 Å resolution, PDB code: 4ARH), zinc bound *Se*ZinT (Zn(II)–*Se*ZinT, at 2.5 Å resolution, PDB code: 4AYH) and zinc bound *Se*ZinT containing a PEG molecule (Zn(II)–*Se*ZinT–PEG, at 2.0 Å resolution, PDB code: 2AW8); all structures are hexagonal ($P6_122$) and contain one molecule in the asymmetric unit.

The analysis of the three *Se*ZinT structures and their comparison with the *Ec*ZinT (YodA) one brings out the following points:

i) The overall fold of *Se*ZinT resembles closely the *Ec*ZinT one, as expected in view of the high sequence identity (71.76%, Fig. 1A). It consists of the calyx domain – an antiparallel up-down β-barrel – and a smaller helical domain. Specifically, the Cα traces of *Se*ZinT and *Ec*ZinT with Ni(II) bound to the Zn(II) binding site (PDB code: 1OEJ) [16] are almost super-imposable. The root-mean square deviation (rmsd) is 0.375 Å (Fig. 1B) despite the occurrence of differences in the flexible parts, especially in the 128–135 loop (Fig. 1C). The His-rich N-terminal tail – HGHHAHG – is not visible, pointing to its high flexibility, as in all the ZinT structures solved thus far. In particular, the average B factor of the last three visible residues (8–10) is much higher than that calculated over the whole structure, *e.g.* >45 Å^2 as compared to 27 Å^2 for Zn(II)–*Se*ZinT.

ii) *Se*ZinT as purified does not contain Zn(II) and hence represents the first metal-free ZinT structure available. In Zn(II)–*Se*ZinT, only one Zn(II) is bound at the end of a hydrophobic pocket at the interface between the calyx and the helix domain (Fig. 1D), namely in the same position as cadmium, nickel and zinc in *Ec*ZinT (PDB codes: 1OEE, 1OEJ, 1OEK and 1S7D, respectively) [16].
Zn(II) binding gives rise to limited conformational changes as apparent from the superimpositions of the Zn(II)–*Se*ZinT and Zn(II)–*Se*ZinT–PEG Cα traces with that of *Se*ZinT (rmsd of 0.248 Å and 0.237 Å, respectively). The flexible 128–135 loop is the only region which displays different conformations in the three structures. However, limited movements are apparent also in the Zn(II) binding site of Zn(II)–*Se*ZinT where the metal is coordinated by His153 (NE2–Zn(II) distance of 2.19 Å), His155 (NE2–Zn(II) distance of 2.41 Å), His144 (NE2–Zn(II) distance of 2.93 Å) and a water molecule (O–Zn(II) distance of 2.96 Å). As shown in Fig. 2A, His155 and His153, the two histidine residues placed at a canonical ligation distance from the metal, undergo a small movement; in particular His153 shifts by 1.9 Å toward Zn(II). In Zn(II)–ZinT–PEG (Fig. 2B), the metal appears to be coordinated tetrahedrally by His153 (NE2–Zn(II) distance of 2.73 Å), His155 (NE2–Zn(II) distance of 2.60 Å), His144 (NE2–Zn(II) distance of 2.48 Å) and an oxygen of the PEG molecule (O–Zn(II) distance of 2.55 Å). No conformational changes are apparent relative to the metal-free structure.
To allow a detailed comparison of the metal coordination shell in *Se*ZinT and *Ec*ZinT, a description of the metal binding site in *Ec*ZinT is in order. Two Zn(II) are present in the 1OEK and 1S7D structures, in which one metal ion is coordinated by His144 and His155, whereas the other interacts with His153, His193, and the carboxyl moiety of Glu189. Several water molecules lie in close contact with the zinc ions, but no precise description of the coordination geometry is given due to local disorder. In the cadmium bound structure (PDB code: 1OEE), the metal is coordinated by three histidine side chains (His144, His153, and His155, from strands F and G of the calyx domain) and three water molecules in a typical octahedral geometry. In the nickel bound form of *Ec*ZinT (PDB code: 1OEJ), the metal is bound to His144, His153, and His155 like Cd(II). All the solved *Ec*ZinT structures also contain metal bound to the protein surface.
Whereas the metal coordination shell and the position of bound Zn(II) in *Se*ZinT resemble those of Ni(II), and Cd(II) bound to *Ec*ZinT (Fig. 2C), the mode of Zn(II) binding differs in the two proteins (Fig. 2D). In the *Ec*ZinT structure, two Zn(II) are placed in the canonical binding pocket as just described, most likely because the crystals were obtained at 200 mM [16], a very high concentration as compared to 5 mM Zn(II) used to grow the Zn(II)–*Se*ZinT crystals and to the sub-millimolar concentrations typical of physiological conditions. As shown below, fluorescence titrations of *Se*ZinT with Zn(II) provide evidence that the protein binds only one Zn(II) with high affinity.

iii) Surprisingly, in the Zn(II)–*Se*ZinT–PEG crystal, a PEG molecule is present in the cavity between the calyx and the helical domain, that is lined with hydrophobic residues like Phe157 and Trp173 (Fig. 3). Two different PEG conformations (A and B), each with

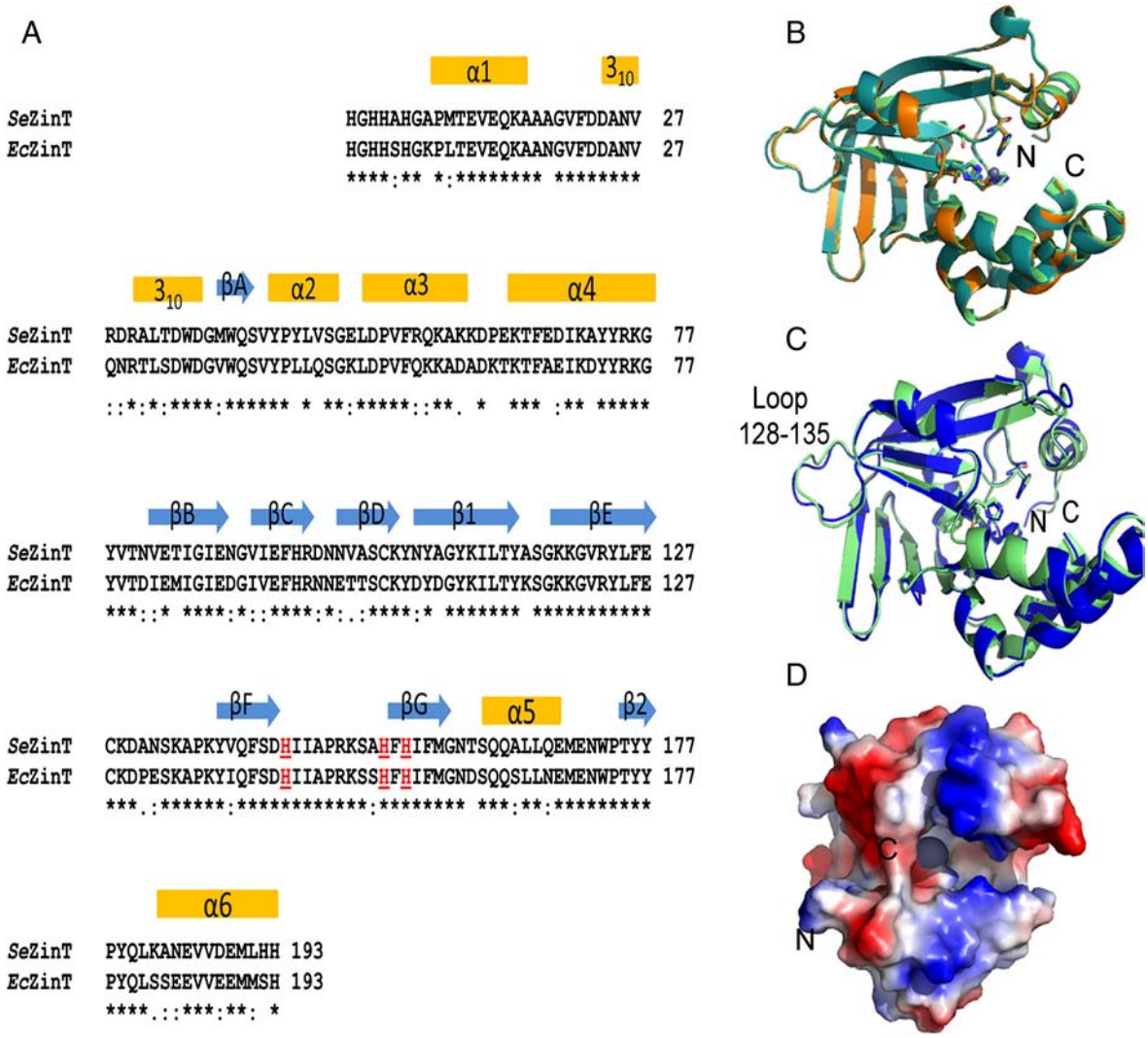

Fig. 1. Structural features of *S. enterica* ZinT. In (A), sequence alignment of *Ec*ZinT and *Se*ZinT. The secondary structure elements are indicated. The Zn(II) coordinating residues are underlined. Identical residues are indicated by asterisks, those defined as similar and more similar by the ClustalW2 program [23] are indicated by '.' and by ':', respectively. In (B), overall fold. *Se*ZinT (PDB code: 4ARH) is colored green, Zn(II)–*Se*ZinT (PDB code: 4AYH) orange, and Zn(II)–*Se*ZinT–PEG (PDB code: 4AW8) blue marine. The zinc ions and the coordinating histidines are indicated. In (C), superimposition between *Se*ZinT and native *Ec*ZinT (PDB code: 1OEJ). *Se*ZinT is colored green and *Ec*ZinT blue. In (D), electrostatic surface of Zn(II)–*Se*ZinT, the bound zinc is represented as a gray sphere. The figures were prepared using PyMol [49].

0.5 occupancy, could be modeled in the protein cavity as the PEG molecule is not bound tightly to the protein. The A conformation is more stable due to binding of PEG to the zinc ion (O8–Zn(II) = 2.55 Å) and to formation of a hydrogen bond with Tyr115 (OH–O14 = 3.1 Å). In the B conformation the PEG molecule is hydrogen bonded only to His144, one of the zinc ligands. It may be surmised that the presence of the long and hydrophobic PEG molecule in the cavity between the two *Se*ZinT domains mimics the *Se*ZnuA His-rich loop in the *Se*ZinT–*Se*ZnuA complex (see below).

3.2. Zinc affinity

The affinity of *Se*ZinT for Zn(II) was assessed by means of fluorescence titrations since Trp173, one of the three Trp residues, is located near the zinc binding site in the crystal structure. Indeed, the intrinsic protein fluorescence (λ_{max} 340 nm) increases as a function of added Zn(II). Consistent with the structural data, the normalized *Se*ZinT fluorescence intensity measured in 20 mM HEPES, 10 mM NaCl, pH 7.5, plotted as a function of added Zn(II), points to binding of one Zn(II)/molecule (Fig. 4A). A very low dissociation constant (22 ± 2 nM) indicative of high affinity binding ($K_A = 4.5 \times 10^7\ M^{-1}$) was obtained by fitting these data with the equation:

$$C = 0.5(C_0 - L_T - K_D) + 0.5\left((C_0 - L_T - K_D)^2 + 4K_D C_0\right)^{0.5}$$

where C is the concentration of metal-free ZinT, C_0 is the total protein concentration, L_T is the total zinc concentration and K_D is the dissociation constant of the ion from the protein.

The affinity of *Se*ZnuA for Zn(II) was determined as well given the paucity of available information. Since the protein intrinsic fluorescence does not change upon addition of Zn(II), an indirect titration method in the presence of the indicator MF was employed [19]. The decrease in absorbance of the indicator was followed as a function of added Zn(II) at 366 nm. The titration curve (Fig. 4B) displays an initial region of constant absorbance until about one equivalent of Zn(II)/*Se*ZnuA is added, and thus indicates that *Se*ZnuA outcompetes MF for available Zn(II). With increase in concentration of added Zn(II), the 366 nm absorbance decreases with a sigmoidal shape characterized by an inflection point at about 45 μM added Zn(II). One can infer that *Se*ZnuA possesses one Zn(II) binding site endowed with a higher affinity for the

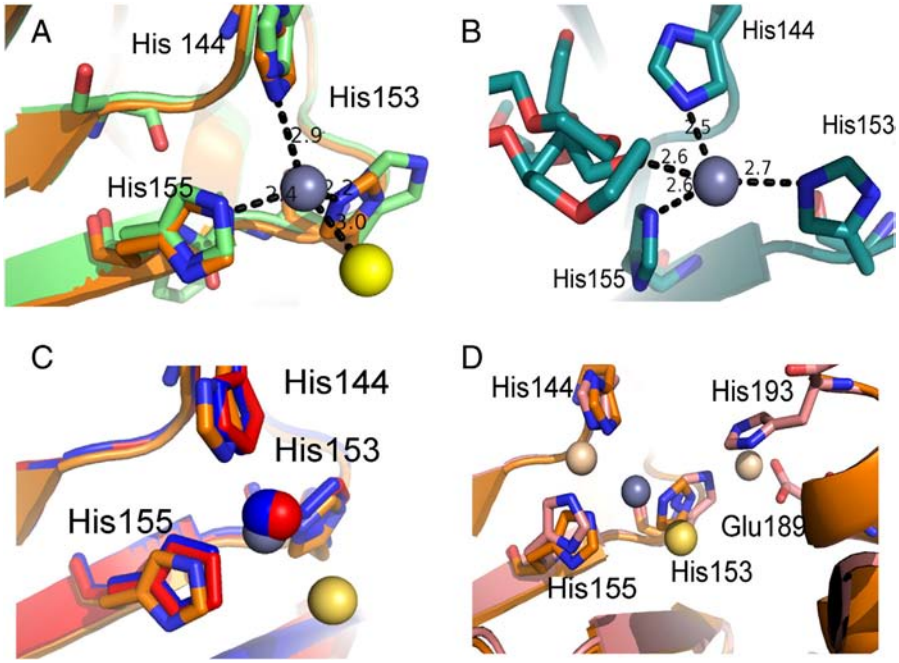

Fig. 2. Zn(II) binding site of *S. enterica* ZinT. In (A), superimposed binding site in metal-free *Se*ZinT (green) and Zn(II)–*Se*ZinT (orange). The coordinating residues and the distances from the metal are indicated. Zn(II) is colored gray and the coordinating water molecule yellow. In (B), binding site in Zn(II)–*Se*ZinT–PEG. The coordinating residues, the PEG molecule and the distances from the metal are indicated. Zn(II) is colored gray. The figure is rotated about 90° around His144 with respect to (A). In (C), superimposed binding site in Cd(II)–*Ec*ZinT, in red, Ni(II)–*Ec*ZinT, in blue, and in Zn(II)–*Se*ZinT, in orange. Zn(II) is depicted in gray, Ni(II) in blue and Cd(II) in red. In (D), superimposed Zn(II) binding site of Zn(II)–*Ec*ZinT, in pink, and Zn(II)–*Se*ZinT, in orange.

metal than MagFura2 ($K_D < 20$ nM) and a second site of affinity in the micromolar range. A similar situation has been described for the two Zn(II) binding sites in *E. coli* ZnuA [19].

3.3. SeZnuA–SeZinT interaction

Gel filtration experiments by Petrarca et al. [10] reported that *Se*ZinT and *Se*ZnuA do not interact when metal-free, but give rise to a 1:1 complex in the presence of Zn(II). To gain further information on the conditions required for complex formation, the *Se*ZinT–*Se*ZnuA system was analyzed by sedimentation velocity in 20 mM HEPES, 10 mM NaCl, pH 7.5 (Table 2). A 1:1 mixture (on a molar basis) of metal-free *Se*ZnuA and *Se*ZinT sediments at an intermediate velocity ($s_{20,w} = 2.5$ S) relative to the isolated proteins indicating that no interaction takes place in accordance with the Petrarca et al. data [10]. When the respective high affinity Zn(II) binding sites are saturated, *Se*ZnuA and *Se*ZinT sediment with an $s_{20,w}$ value of 3.2 S, consistent with formation of a 1:1 *Se*ZnuA–*Se*ZinT complex. To establish the dependence of complex formation on the metallation state of the two partner proteins, 1:1 molar mixtures were analyzed in which only one protein contained Zn(II). Importantly, when Zn(II)–*Se*ZinT is mixed with apo-*Se*ZnuA, the $s_{20,w}$ value (3.15 S) points to formation of a 1:1 complex. In contrast, no interaction takes place when apo-*Se*ZinT is mixed with *Se*ZnuA containing one Zn(II)/molecule so as to saturate the high affinity binding site ($s_{20,w} = 2.60$ S). It follows that formation of the *Se*ZinT–*Se*ZnuA complex is governed by the metallation state of *Se*ZinT.

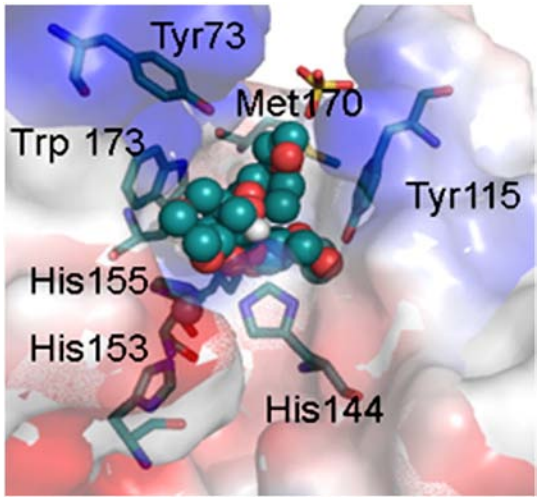

Fig. 3. Electrostatic surface and Zn(II) binding cavity in Zn(II)–*Se*ZinT–PEG. The PEG molecule is represented as spheres. The residues interacting with PEG and the three Zn(II) coordinating histidines are represented as sticks.

Many attempts have been made to obtain X-ray quality crystals of the *Se*ZinT–*Se*ZnuA complex. The complex has been isolated, purified by gel chromatography [10] and crystallized in the absence and in the presence of added Zn(II). More than 600 crystallization conditions have been explored with a high-throughput screening method using a crystallization robot. In the presence of added Zn(II), crystals diffracting only at very low resolution were obtained. Therefore, structural information on the mode of interaction between *Se*ZinT and *Se*ZnuA was gained by means of SAXS experiments on the purified complex.

The scattering curves computed from different dilutions in the range 0.17 to 5.0 mg/ml showed significant concentration dependency below 2.5 mg/ml, suggesting the occurrence of dissociation. Hence, only the curves between 2.5 and 5 mg/ml were used for the analysis that yielded the overall parameters presented in Table 3. The $P(r)$ function shows a bell shape typical for globular or slighlty elongated proteins and yields a D_{max} of ~85 Å (Fig. 5A). *Ab initio* model reconstruction using DAMMIF/DAMAVER (NSD = 0.628 ± 0.05) yields an estimated molecular mass of ~38 kDa. This value agrees with other independent molecular mass estimations based on the Porod volume (~37 kDa) as well as on the forward scattering $I(0)$ (~43 kDa), whereas the expected value of the *Se*ZinT–*Se*ZnuA complex is 53.2 kDa. A molecular mass

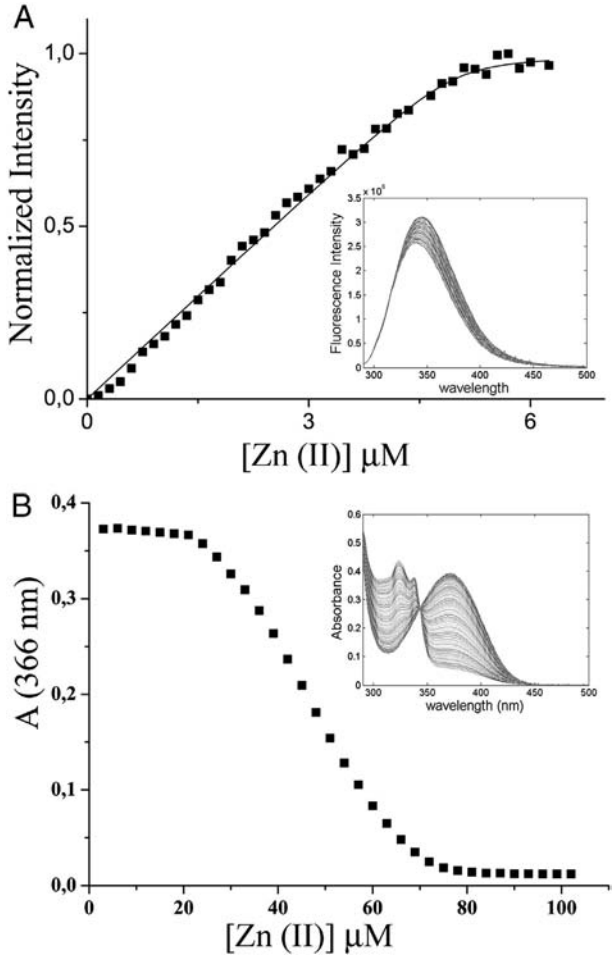

Fig. 4. Determination of the affinity for Zn(II) of *S. enterica* ZinT (A) and *S. enterica* ZnuA (B). In (A), fluorescence titration of *Se*ZinT with Zn(II). Experimental data expressed as $I - I_{max}/I_{max} - I_{min}$ and plotted as a function of the total zinc concentration added. I is the fluorescence intensity at 340 nm, I_{max} and I_{min} are, respectively, the maximum and minimum values measured during the titration. The continuous line represents the fit to the data yielding a K_D value of 22 ± 2 nM. In (B), titration of *Se*ZnuA with Zn(II) in the presence of the indicator Mag-Fura-2. The absorbance of the indicator at 360 nm is plotted as a function of the total zinc concentration added. For details see under Material and methods.

value of 38–40 kD can be accounted for by assuming that a finite equilibrium is established between the *Se*ZinT–*Se*ZnuA complex and the two isolated proteins. In particular, at the protein concentrations used for the analysis ($4.7–9.4 \times 10^{-5}$ M), the experimental molecular mass is obtained by assuming that *Se*ZinT–*Se*ZnuA and the isolated proteins are in a molar ratio of 2:1:1. On this basis, the value of the equilibrium constant, K_D, is around 10^{-5} M.

Table 2
Sedimentation velocity experiments on *Se*ZinT and *Se*ZnuA and their equimolar mixtures in their apo- and Zn(II)-bound forms.

Protein	$s_{20,W}$ (S)
Zn(II)–*Se*ZnuA	2.70
Apo-*Se*ZnuA	2.70
Zn(II)–*Se*ZinT	2.40
Apo-*Se*ZinT	2.40
Apo-*Se*ZinT + apo-*Se*ZnuA	2.50
Zn(II)–*Se*ZinT + Zn(II)–*Se*ZnuA	3.20
Zn(II)–*Se*ZinT + apo-*Se*ZnuA	3.15
Apo-*Se*ZinT + Zn(II)–*Se*ZnuA	2.50
Zn(II)–*Se*ZinT + Zn(II)–*Se*ZnuA Δ118–141	2.70

The $s_{20,W}$ values represent the average of at least two experiments.

Table 3
Data collection and SAXS-derived parameters for the *Se*ZinT–*Se*ZnuA complex.

Data-collection parameters	
Instrument (detector)	PILATUS 1 M pixel (67×420 mm^2)
Beam geometry	0.7×0.7 mm^2
Wavelength (Å)	0.931
s range (nm^{-1})	0.05–4.5
Exposure time (s)	1
Concentration range (mg ml^{-1})	2.5–5
Temperature (K)	277.15
Structural parameters	
$I(0)$ (cm^{-1}) [from $P(r)$]	45.550
R_g (nm) [from $P(r)$]	2.5 ± 0.2
$I(0)$ (cm^{-1}) [from Guinier approximation]	45.524
R_g (nm) [from Guinier approximation]	2.5 ± 0.2
D_{max} (nm)	8.5 ± 0.5
Porod volume estimate (Å^3)	55 ± 5
Dammif excluded volume (Å^3)	76.4 ± 5
Molecular-mass determination	
Molecular mass M_r (kDa) [from *Porod invariant*]	37 ± 5
Molecular mass M_r (kDa) [from *excluded volume*]	38 ± 5
Molecular mass M_r (kDa) [from $I(0)$]	43 ± 10
Software employed	
Primary data reduction	PIPELINE
Data processing	PRIMUS
Ab initio analysis	DAMMIF
Validation and averaging	DAMAVER
Rigid-body modeling	MASSHA
Computation of model intensities	CRYSOL
Three-dimensional representations	VMD

Lastly, quaternary structure of the *Se*ZnuA–*Se*ZinT complex derived from rigid body modeling of *Se*ZinT (PDB code: 4ARH) and *Se*ZnuA (PDB code: 2XQV) and shown in Fig. 5A has the lowest discrepancy ($\chi = 1.148$) relative to the experimental data and a full compatibility with the *ab initio* reconstruction (Fig. 5B). The calculated molecular envelope in Fig. 5B displays an ellipsoidal shape that fits well with the formation of a 1:1 complex between the two proteins. In turn, the model depicted in Fig. 5C indicates that the Zn(II) binding sites of both proteins face the complex interface and that the His-rich loop is keyed in the ZinT cavity between the calyx and the helical domain in a similar position as the PEG molecule (Fig. 5C). The observation that the Zn(II)–*Se*ZnuA mutant devoid of the His-rich 118–141 loop (Zn(II)–*Se*ZnuA Δ118–141) does not form a stable complex with (Zn)–*Se*ZinT (Table 2) validates this indication.

4. Discussion

The multiplicity of physico-chemical techniques employed to characterize *Se*ZinT reveals key structural features that are relevant to the role this protein plays in the management of periplasmic Zn(II) in addition to the major player, the high affinity uptake protein *Se*ZnuA.

Three different X-ray *Se*ZinT structures were solved, namely the apo-protein structure, the first available one, the Zn(II)-bound form, and a further Zn(II)-bound structure of likely physiological relevance that contains a PEG molecule. *Se*ZinT displays the same two-domain architecture of *Ec*ZinT, as expected on the basis of the high sequence identity (Fig. 1) and likewise possesses one high affinity Zn(II) binding site, located at the end of the hydrophobic cavity formed between the calyx and the helical domain. In *Se*ZinT, Zn(II) is bound in the same position as Cd(II) and Ni(II) in *Ec*ZinT [16]. However, the Zn(II) coordination differs. In *Se*ZinT, Zn(II) is bound with tetrahedral coordination by three histidine residues from strands F and G of the calyx domain: His153 and His155 placed at a canonical coordination distance from the metal (2.2 and 2.4 Å), and His 144 at about 3.0 Å from Zn(II). The fourth ligand, an oxygen atom, is provided by a water molecule. The binding of Zn(II) causes only slight movements limited to the coordinating histidine ligands; in particular His153 is shifted by 1.9 Å toward the cavity, suggesting that this residue may participate in

the Zn(II) management process. The PEG–Zn(II)*Se*ZinT structure, as alluded to above, is of special interest as it shows that the Zn(II) binding cavity between the calyx and the helical domain can harbor a long, single-chain polymer (Fig. 3). In a functional context, this can be envisaged to be part of the *Se*ZnuA His-rich loop in accord with the SAXS-derived model of the *Se*Zint–*Se*ZnuA complex. In the model, the

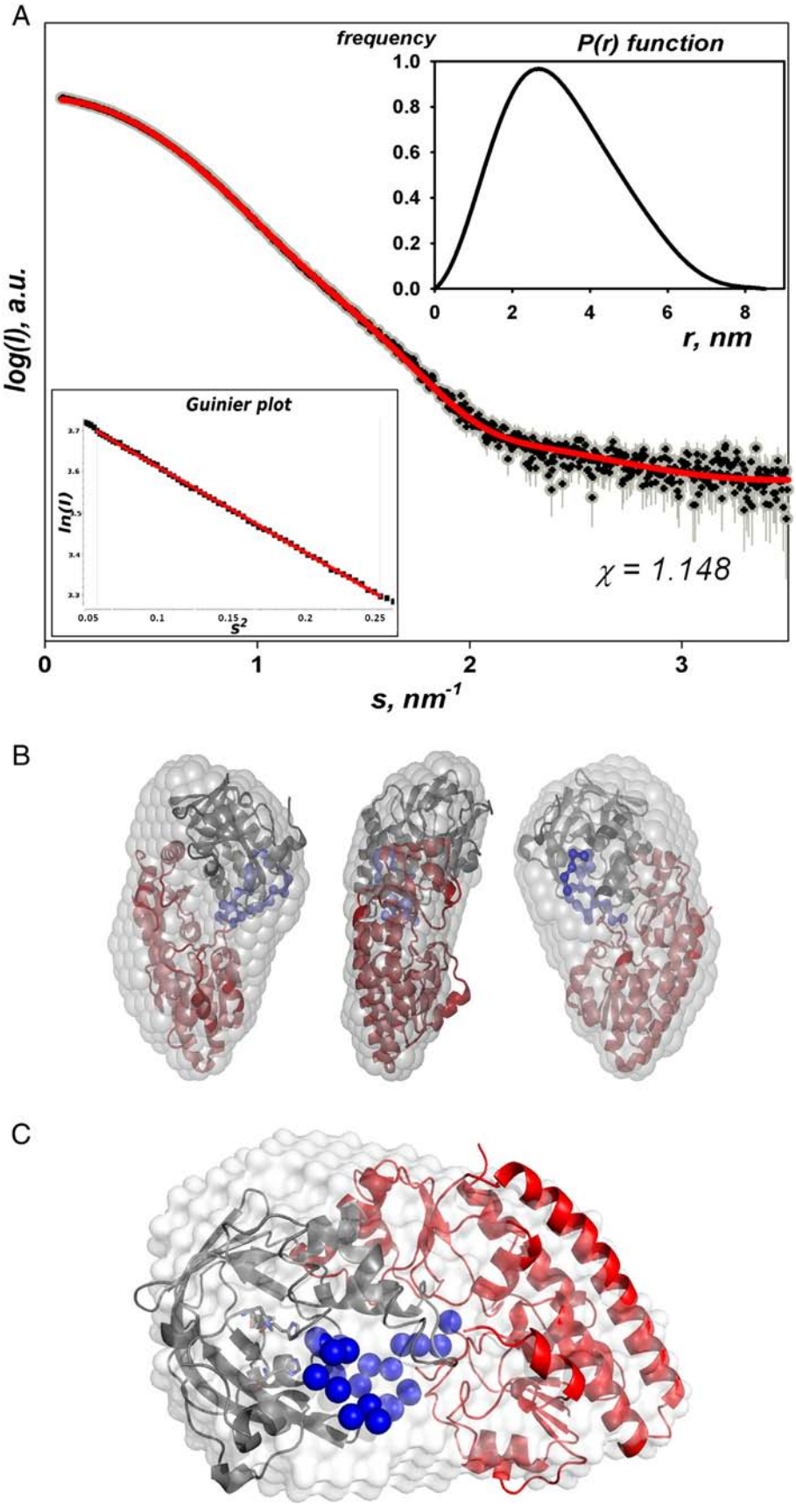

Zn(II) binding sites of the two proteins are juxtaposed and the ZnuA His-rich loop enters the *Se*ZinT cavity between the calyx and the helical domain, just like the PEG molecule (Fig. 5C). This picture can be expanded to encompass the relative affinities of *Se*Zint and *Se*ZnuA for Zn(II). Based on the respective titration curves (Fig. 4A and B), *Se*ZinT binds one Zn(II) with high affinity (K_D 22 ± 2 nM), whereas *Se*ZnuA binds two Zn(II) with significantly different affinity. The first site is characterized by a higher affinity for Zn(II) than the indicator MagFura2 (K_D<20 nM). The affinity of the second site can be estimated to lie in the micromolar range. Titrations of *Se*ZnuA bound to a fluorescent probe [46] likewise pointed to the presence of two Zn(II) binding sites. Their analysis yielded a K_D ~ 1 μM for the low affinity site, but did not allow measurement of the K_D value pertaining to the high affinity one. The *Se*ZnuA structures solved by Ilari et al. [13] suggest that the low affinity site is likely to be located on the His-rich loop.

The studies on *Salmonella* indicate that *Se*ZinT transfers Zn(II) to *Se*ZnuA and in so doing acts as an accessory member of the ZnuABC transport system [10,11]. This contention requires that *Se*ZinT has a lower affinity for Zn(II) than ZnuA and that the two proteins form a complex solely when Zn(II) is bound to *Se*ZinT. The affinity data just discussed and those on formation of the *Se*ZinT–*Se*ZnuA complex (Table 2) show that both requirements are met. The SAXS experiments add information on the stability of the complex. The estimated molecular mass, using both the excluded and the Porod volume, is 38–40 kDa, as compared to the calculated value of 53 kDa. This difference can be accounted for by assuming that the *Se*ZnuA–*Se*ZinT complex and the two partner proteins are in a 2:1:1 ratio, when the protein concentration is 9.0×10^{-5} M. This finding is consistent with an affinity constant of about 10^5 M^{-1}. It is worth recalling that the gel filtration experiments by Petrarca et al. [10] likewise indicated that the complex is in equilibrium with *Se*ZinT and *Se*ZnuA, but did not estimate the equilibrium constant. The SAXS data also provide information on the structural relationship between the two proteins in the complex. The model with the lowest discrepancy relative to the experimental data (Fig. 5C) indicates that the Zn(II) binding sites of both proteins face each other at the complex interface. It appears therefore that *Se*ZinT and *Se*ZnuA are in a structural relationship that allows Zn(II) to be transferred from Zn(II)*Se*ZinT to *Se*ZnuA, likely *via* the His-rich loop.

One may ask why *Salmonella* expresses ZinT since binding of periplasmic Zn(II) to ZnuA would be favored thermodynamically. It is well established [2] that the thermodynamics of metal binding *in vitro* does not describe fully the mechanisms operating in bacterial cells to ensure that each metallo-protein acquires the correct metal. On this basis, the presence of two structurally distinct periplasmic metal binding transporters (*Se*ZnuA and *Se*ZinT) can be expected to be more advantageous than increasing the concentration of a single one (*Se*ZnuA). Thereby the bacterium can increase the ability to obtain Zn(II) from the surface of different proteins, where the metal is known to bind tightly in a rather unspecific manner. It is worth noting that recent studies have shown that the production of multiple proteins involved in zinc uptake is not limited to bacteria expressing ZinT. For example, *Listeria monocytogenes* expresses two ABC-type Zinc importers, both contributing to full virulence [47], while in *Streptococcus pneumoniae* the zinc importer AdcAII (a ZnuA homologue) can form a complex with the zinc-binding surface protein PhtD, suggesting that this interaction contributes to the efficiency of the zinc uptake mechanism [48].

In conclusion, the present data contribute significantly to the understanding of the periplasmic zinc transport mechanism mediated by the ZnuABC ATP binding cassette in Gram-negative bacteria. They lend support to the hypothesis of Petrarca et al. [10] that *Se*ZinT binds Zn(II) in the periplasmic space and contributes to metal transport by transferring the metal to *Se*ZnuA that delivers it to ZnuB. Consequently, *Se*ZinT can be considered an accessory component of the ZnuABC transporter that enhances the ability of ZnuA to recruit Zn(II) under conditions characterized by very low metal availability like those encountered by *S. enterica* within the infected host.

Acknowledgements

The authors gratefully acknowledge a grant from Fondazione Roma and funding from the European Community's Seventh Framework Programme (FP7/2007–2013) under BioStruct-X (grant agreement N° 283570) and Bag Project 1223.8. They thank HZB (Helmholtz Zentrum Berlin) for allocation of synchrotron radiation beam-time and the European Synchrotron Radiation Facility (ESRF) for providing synchrotron radiation for the SAXS experiments at beamline BM29. F.A. was a recipient of a fellowship from Fondazione Roma. The authors thank Dr. Annarita Fiorillo for the SAXS mearurements.

References

[1] H. Irving, R.J.P. Williams, Order of stability of metal complexes, Nature 162 (1948) 746–747.
[2] K.J. Waldron, N.J. Robinson, How do bacterial cells ensure that metalloproteins get the correct metal? Nat. Rev. Microbiol. 7 (2009) 25–35.
[3] C.E. Outten, F.W. Outten, T.V. O'Halloran, DNA distortion mechanism for transcriptional activation by ZntR, a Zn(II)-responsive MerR homologue in *Escherichia coli*, J. Biol. Chem. 274 (1999) 37517–37524.
[4] D. Wang, T.K. Hurst, R.B. Thompson, C.A. Fierke, Genetically encoded ratiometric biosensors to measure intracellular exchangeable zinc in *Escherichia coli*, J. Biomed. Opt. 16 (2011) 087011.
[5] K. Hantke, Bacterial zinc uptake & regulators, Curr. Opin. Microbiol. 8 (2005) 196–202.
[6] E.M. Panina, A.A. Mironov, M.S. Gelfand, Comparative genomics of bacterial zinc regulons: enhanced ion transport, pathogenesis, and rearrangement of ribosomal proteins, Proc. Natl. Acad. Sci. 100 (2003) 9912–9917.
[7] P. Ferianc, A. Farewell, T. Nystrom, The cadmium-stress stimulon of *Escherichia coli* K-12, Microbiology 144 (1998) 1045–1050.
[8] C.J. Kershaw, N.L. Brown, J.L. Hobman, Zinc dependence of *zinT* (*yodA*) mutants and binding of zinc, cadmium and mercury by ZinT, Biochem. Biophys. Res. Commun. 364 (2007) 66–71.
[9] A.I. Graham, S. Hunt, S.L. Stokes, N. Bramall, J. Bunch, A.G. Cox, C.W. McLeod, R.K. Poole, Severe zinc depletion of *Escherichia coli*: roles for high affinity zinc binding by Zint, zinc transport and zinc-independent proteins, J. Biol. Chem. 284 (2009) 18377–18389.
[10] P. Petrarca, S. Ammendola, P. Pasquali, A. Battistoni, The Zur-regulated ZinT protein is an auxiliary component of the high affinity ZnuABC zinc transporter that maximizes metal recruitment during severe zinc shortage, J. Bacteriol. 192 (2010) 1553–1564.
[11] R. Gabbianelli, R. Scotti, S. Ammendola, P. Petrarca, L. Nicolini, A. Battistoni, Role of ZnuABC and ZinT in *Escherichia coli* O157:H7 zinc acquisition and interaction with epithelial cells, BMC Microbiol. 11 (2011) 36–47.
[12] A. Dintilhac, G. Alloing, C. Granadel, J.P. Claverys, Competence and virulence of *Streptococcus pneumoniae*: Adc and PsaA mutants exhibit a requirement for Zn and Mn resulting from inactivation of putative ABC metal permeases, Mol. Microbiol. 25 (1997) 727–739.
[13] A. Ilari, F. Alaleona, P. Petrarca, A. Battistoni, E. Chiancone, The X-ray structure of the zinc transporter ZnuA from *Salmonella enterica* discloses a unique triad of zinc-coordinating histidines, J. Mol. Biol. 409 (2011) 630–641.
[14] M. Falconi, F. Oteri, S. Di Palma, A. Pandey, A. Battistoni, A. Desideri, Structural–dynamical investigation of the ZnuA histidine-rich loop: involvement in zinc management and transport, J. Comput. Aided Mol. Des. 25 (2011) 181–194.
[15] S. Ammendola, P. Pasquali, C. Pistoia, P. Petrucci, P. Petrarca, G. Rotilio, A. Battistoni, The high affinity Zn^{2+} uptake system ZnuABC is required for bacterial zinc homeostasis in intracellular environments and contributes to virulence of *Salmonella enterica*, Infect. Immun. 75 (2007) 5867–5876.
[16] G. David, K. Blondeau, M. Schiltz, S. Penel, A. Lewit-Bentley, YodA from *Escherichia coli* is a metal-binding, lipocalin-like protein, J. Biol. Chem. 278 (2003) 43728–43735.
[17] B.R. Chandra, M. Yogavel, A. Sharma, Structural analysis of ABC-family periplasmic zinc binding protein provides new insights into mechanism of ligand uptake and release, J. Mol. Biol. 367 (2007) 970–987.

Fig. 5. SAXS analysis for the *Se*ZnuA–*Se*ZinT complex. In (A), experimental SAXS intensity profiles (logarithmic) for the *Se*ZnuA–*Se*ZinT complex (black dot) *vs.* CRYSOL computed theoretical scattering (red line). The figure also shows the linearity of the Guinier region as well as the derived pair-distance distribution function $P(r)$. In (B), *Se*ZnuA–*Se*ZinT interaction as derived from rigid body modeling. *Se*ZnuA (red, PDB code: 2XQV) and *Se*ZinT (black, PDB code: 4ARH) assemble into a rather globular complex fully compatible with the *ab initio* shape computed from experimental data only using DAMMIF/DAMAVER (gray). The missing loop *Se*ZnuA Δ118–141 (blue) was reconstructed using BUNCH. ZnuA is colored red, the reconstructed His rich loop is colored blue and ZinT is colored in gray. In (C), blow-up of the Se–ZnuA–SeZinT complex interface. ZnuA is colored red, the reconstructed His rich loop is colored blue and ZinT is colored in gray.

[18] H. Li, G. Jogl, Crystal structure of the zinc-binding transport protein ZnuA from *Escherichia coli* reveals an unexpected variation in metal coordination, J. Mol. Biol. 368 (2007) 1358–1366.
[19] L.A. Yatsunyk, J.A. Easton, L.R. Kim, S.A. Sugarbaker, B. Bennett, R.M. Breece, I.I. Vorontsov, D.L. Tierney, M.W. Crowder, A.C. Rosenzweig, Structure and metal binding properties of ZnuA, a periplasmic zinc transporter from *Escherichia coli*, J. Biol. Inorg. Chem. 13 (2008) 271–288.
[20] S. Banerjee, B. Wei, M.B. Pakrasi, H.B. Pakrasi, T.J. Smith, Structural determinants of metal specificity in the zinc transport proteins ZnuA from *Synechocystis 6803*, J. Mol. Biol. 333 (2003) 1061–1069.
[21] U. Müller, N. Darowski, M.R. Fuchs, R. Förster, M. Hellmig, K.S. Paithankar, S. Pühringer, M. Steffien, G. Zocher, M.S. Weiss, Facilities for macromolecular crystallography at the Helmholtz-Zentrum Berlin, J. Synchrotron Radiat. 19 (2012) 442–449.
[22] Z. Otwinowski, W. Minor, Processing of X-ray diffraction data collected in oscillation mode, Methods Enzymol. 276 (1997) 307–332.
[23] A.G.W. Leslie, H.R. Powell, Processing diffraction data with MOSFLM, in: R. Read, J.L. Sussman (Eds.), Evolving Methods for Macromolecular Crystallography, The Netherlands NATO Series II, 245, Springer, Dordrecht, 2007, pp. 41–51.
[24] M.A. Larkin, G. Blackshields, N.P. Brown, R. Chenna, P.A. McGettigan, H. McWilliam, F. Valentin, I.M. Wallace, A. Wilm, R. Lopez, J.D. Thompson, T.J. Gibson, D.G. Higgins, ClustalW and ClustalX version 2, Bioinformatics 23 (2007) 2947–2948.
[25] A. Vagin, A. Teplyakov, MOLREP: an automated program for molecular replacement, J. Appl. Crystallogr. 30 (1997) 1022–1025.
[26] M.D. Winn, C.C. Ballard, K.D. Cowtan, E.J. Dodson, P. Emsley, P.R. Evans, R.M. Keegan, E.B. Krissinel, A.G.W. Leslie, A. McCoy, S.J. McNicholas, G.N. Murshudov, N.S. Pannu, E.A. Potterton, H.R. Powell, R.J. Read, A. Vagin, K.S. Wilson, Overview of the CCP4 suite and current developments, Acta Crystallogr. D67 (2011) 235–242.
[27] G.N. Murshudov, A.A. Vagin, E.J. Dodson, Refinement of macromolecular structures by the maximum-likelihood method, Acta Crystallogr. D Biol. Crystallogr. 53 (1997) 240–255.
[28] P. Emsley, K. Cowtan, Coot: model-building tools for molecular graphics, Acta Crystallogr. D Biol. Crystallogr. 60 (2004) 2126–2132.
[29] R.A. Laskowski, M.W. MacArthur, D.S. Moss, J.M. Thornton, PROCHECK: a program to check the stereochemical quality of protein structures, J. Appl. Crystallogr. 26 (1993) 283–291.
[30] G.K. Walkup, B. Imperiali, Design and evaluation of a peptidyl fluorescent chemosensor for divalent zinc, J. Am. Chem. Soc. 119 (1996) 3443–3450.
[31] K.E. Dineley, L.M. Malaiyandi, I.J. Reynolds, A reevaluation of neuronal zinc measurements: artifacts associated with high intracellular dye concentration, Mol. Pharmacol. 62 (2002) 618–627.
[32] P. Pernot, P. Theveneau, T. Giraud, R. Nogueira Fernandes, D. Nurizzo, D. Spruce, J. Surr, S. McSweeney, A. Round, F. Felisaz, L. Foedinger, A. Gobbo, J. Huet, C. Villard, F.P. Cipriani, New beamline dedicated to solution scattering from biological macromolecules at the ESRF, J. Phys. Conf. Ser. 247 (2010) 012009.
[33] A.R. Round, D. Franke, S. Moritz, R. Huchler, M. Fritsche, D. Malthan, R. Klaering, D.I. Svergun, M. Roessle, Automated sample-changing robot for solution scattering experiments at the EMBL Hamburg SAXS station X33, J. Appl. Crystallogr. 41 (2008) 913–917.
[34] A. Guinier, La diffraction des rayons X aux tres petits angles; application a l'etude de phénomènes ultramicroscopiques, J. Physiol. Paris 12 (1939) 161–237.
[35] P.V. Konarev, V.V. Volkov, A.V. Sokolova, M.H.J. Koch, D.I. Svergun, PRIMUS: a Windows PC-based system for small-angle scattering data analysis, J. Appl. Crystallogr. 36 (2003) 1277–1282.
[36] M.V. Petoukhov, D. Franke, A.V. Shkumatov, G. Tria, A.G. Kikhney, M. Gajda, C. Gorba, H.D.T. Mertens, P.V. Konarev, D.I. Svergun, New developments in the ATSAS program package for small-angle scattering data analysis, J. Appl. Crystallogr. 45 (2012) 342–350.
[37] D.I. Svergun, Determination of the regularization parameter in indirect-transform methods using perceptual criteria, J. Appl. Crystallogr. 25 (1992) 495–503.
[38] G. Porod, General theory, in: O. Glatter, O. Kratky (Eds.), Small Angle X-ray Scattering, Academic Press, London, 1982.
[39] V.V. Volkov, D.I. Svergun, Uniqueness of ab initio shape determination in small-angle scattering, J. Appl. Crystallogr. 36 (2003) 860–864.
[40] E. Mylonas, D. Svergun, Accuracy of molecular mass determination of proteins in solution by small-angle X-ray scattering, J. Appl. Crystallogr. 40 (2007) 245–249.
[41] D. Franke, D.I. Svergun, DAMMIF, a program for rapid ab-initio shape determination in small-angle scattering, J. Appl. Crystallogr. 42 (2009) 342–346.
[42] P.V. Konarev, M.V. Petoukhov, D.I. Svergun, MASSHA — a graphic system for rigid body modelling of macromolecular complexes against solution scattering data, J. Appl. Crystallogr. 34 (2001) 527–532.
[43] M.V. Petoukhov, D.I. Svergun, Global rigid body modelling of macromolecular complexes against small-angle scattering data, Biophys. J. 89 (2005) 1237–1250.
[44] D.I. Svergun, C. Barberato, M.H.J. Koch, CRYSOL — a program to evaluate X-ray solution scattering of biological macromolecules from atomic coordinates, J. Appl. Crystallogr. 28 (1995) 768–773.
[45] M. Kozin, D. Svergun, Automated matching of high- and low-resolution structural models, J. Appl. Crystallogr. 34 (2001) 33–41.
[46] L. Castelli, P. Stella, A. Petrarca, A. Battistoni, A. Desideri, M. Falconi, Zinc ion coordination as a modulating factor of the ZnuA histidine-rich loop flexibility: a molecular modeling and fluorescence spectroscopy study, Biochem. Biophys. Res. Commun. 430 (2013) 769–773.
[47] D. Corbett, J. Wang, S. Schuler, G. Lopez-Castejon, S. Glenn, D. Brough, P.W. Andrew, J.S. Cavet, I.S. Roberts, Two zinc uptake systems contribute to the full virulence of *Listeria monocytogenes* during growth *in vitro* and *in vivo*, Infect. Immun. 80 (2012) 14–21.
[48] E. Loisel, S. Chimalapati, C. Bougault, A. Imberty, B. Gallet, A.M. Di Guilmi, J. Brown, T. Vernet, C. Durmort, Biochemical characterization of the histidine triad protein PhtD as a cell surface zinc-binding protein of *Pneumococcus*, Biochemistry 50 (2011) 3551–3558.
[49] W.L. DeLano, The PyMOL Molecular Graphics System, DeLano Scientific, San Carlos, CA, 2002.